Article

Formation Mechanism and Improvement of Magnetic Particle Inspection Defects in Cr5 Backup Roller Forged Ingot

Weifeng Zhang [1,2], **Guanbo Wang** [1], **Yanling Zhang** [1,*], **Guoguang Cheng** [1] **and Zhonghua Zhan** [2]

1   State Key Laboratory of Advanced Metallurgy, University of Science and Technology Beijing, Beijing 100083, China; zhangwf@citic-hic.com.cn (W.Z.); owenbread@xs.ustb.edu.cn (G.W.); chengguoguang@metall.ustb.edu.cn (G.C.)
2   Luoyang CITIC HIC Casting and Forging Co., Ltd., Luoyang 471039, China; lyzhan1005@xs.ustb.edu.cn
*   Correspondence: zhangyanling@metall.ustb.edu.cn

Abstract: Industrial tests and thermodynamic calculations were utilized to investigate the source and formation of magnetic particle inspection defects identified on the near-surface of the Cr5 back-up roll forged ingot, which was used in large cold rolling mills. The results showed that the linear aggregating SiO_2-MnO-Al_2O_3 liquid inclusions up to 3 mm led to the flaw detection failure. SiO_2-MnO-Al_2O_3 liquid inclusions were firstly formed in the inductive furnace. Due to its low contact angle, a huge amount of SiO_2-MnO-Al_2O_3 liquid inclusions were inherited into the forged ingot. The formation of SiO_2-MnO-Al_2O_3 liquid inclusions was attributed to the over-oxidation and relatively low aluminum content in the molten steel, as calculated by Factsage 8.1. Controlling the amount of aluminum in molten steel during the smelting process could modify the formation of SiO_2-MnO-Al_2O_3 and CaO-SiO_2-Al_2O_3 liquid oxide into solid Al_2O_3 type inclusions that were easily removed. Besides, the CaO-SiO_2-Al_2O_3 liquid oxide could be transformed from CaO-Al_2O_3 type oxide by the significant loss of aluminum content during the VD process or slag entrapment. Certain content of aluminum in the molten steel could improve the flaw detection caused by the aggregating SiO_2-MnO-Al_2O_3 inclusions effectively.

Keywords: Cr5; back-up roller; forged ingot; large-size inclusions; SiO_2-MnO-Al_2O_3; contact angle; aluminum deoxidation; magnetic particle inspection; defects

1. Introduction

In recent years, rolling mills have been making progress to meet the ever-increasing needs for high-quality steel products, particularly in China. Accordingly, the work roller and back-up roller are required to exhibit superior performance such as exceptional fatigue strength under high load and speed service conditions [1–7].

It is widely recognized that increasing Chromium content could reduce wear loss linearly [8–11]. Therefore, the chromium content of backup rollers has increased from 1.2% up to 3% and 5% in the 1970s [9,12,13]. The appearance of vacuum refining and electro-slag remelting (ESR) technology guaranteed the goal of high carbon with high alloy elements content and achieved the low hydrogen content [13,14]. Adding alloy elements like Mo, V, and W into backup rollers could also promote mechanical properties further as required. Nowadays, backup rollers were classified into Cr3 series and Cr5 series by their chromium content [8,9,15]. Non-destructive testing (NDT) technology, e.g., ultrasonic testing (UT), magnetic particle inspection (MPI), radiographic testing (RT), etc., have been widely used in the industry [16]. MPI was utilized frequently among these methods owing to the demanding requirements of surface and near-surface quality in rollers More and more defects were considered as metallurgical defects, which were caused by inclusions created in deoxidation, reactions between molten steel, slag and refractory, or even slag entrapment [17–24]. Jamil et al. [24] found that alumina and oxide types non-metallic inclusions caused the failure of ultrasonic testing in the sugar mill shaft. Lu et al. [25]

found that large-sized, long-striped MnS inclusions were the major cause of the magnetic particle testing failure in the heavy truck crankshaft. Wang et al. [26] also found that the aggregation of single Al_2O_3 particles and Al_2O_3 clusters existed on the surface of 80 t 20Cr-8Ni stainless ingot, which failed the penetrating testing.

However, the studies aimed at promoting the properties of rollers were mainly around the after-casting manufacturing procedure, e.g., obtaining ideal characteristics of carbides, microstructure by heat treatment, etc. [27–30]. Meanwhile, few studies concerning the evolution and influence of inclusions in the large forged ingots were found [24]. Consequently, combined the appearance of ultrasonic defects on the post-forging rollers with the corresponding specimens during the plant steelmaking process, the origin, evolution, and improvement of defects have been analyzed and clarified. Besides, under the different deoxidation processes, the corresponding evolution and formation mechanism of oxide inclusions aided by thermodynamics calculation and plant trials were discussed as follows.

2. Materials and Methods

2.1. Experimental Procedure

The steelmaking process of 50ton Cr5 type backup roller could be briefly described as "induction furnace (IF) → ladle furnace (LF1) → ladle furnace (LF2) → vacuum degasser (VD) → ladle furnace (LF3) → vacuum casting (VC)", as shown in Figure 1 The return scrap and alloy raw materials were melted in the IF. Then the deoxidation, desulfurization, and composition adjustment took place in LF1, which served as a pre-refining procedure. After the LF2 refining process, the vacuum degasser mainly undertook to degas especially dehydrogenation. Afterward, LF3 was considered to fulfill the final composition adjustment and superheat degree requirements before vacuum casting. To trace the origin of the defects, we implemented the tracking and analysis during the whole metallurgical process. And the original deoxidizer was silicon-aluminum (Si-Al) complex deoxidizer (Si: 65% in mass%, Al: 25% in mass%).

Lollipop steel specimens quenched by water and slag were sampled at different smelting stages i.e., the end of IF smelting, the beginning and end of each LF refining process, the vacuum-breaking of VD, and the beginning of VC, which were named by their chronological order, respectively. The defective parts sampled after forging and fine machining were rechecked and illustrated by a magnetic particle flaw detector, which was processed into 15 mm × 15 mm × 15 mm cubes to achieve the defective location and characteristics by optical microscope, as shown in Figure 2. All the specimens in the smelting process were machined to 10 mm × 10 mm × 10 mm cubes for testing and analysis. Schematic illustrations of the metallurgical process and sampling were shown in Figure 1.
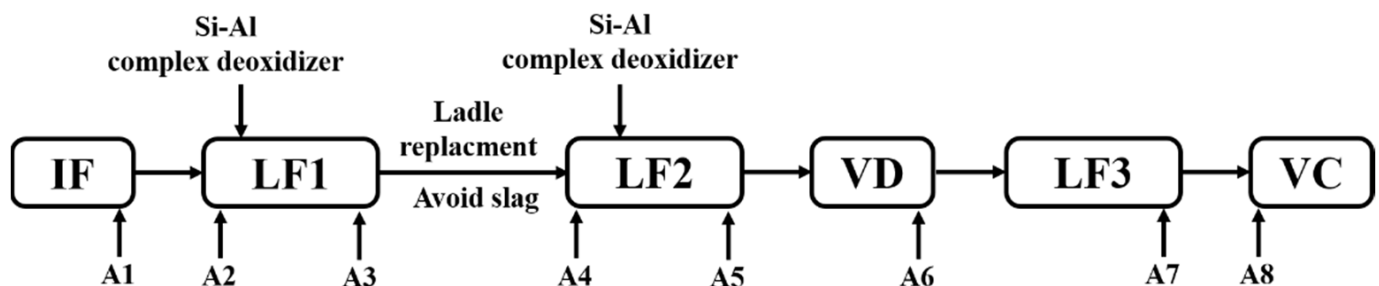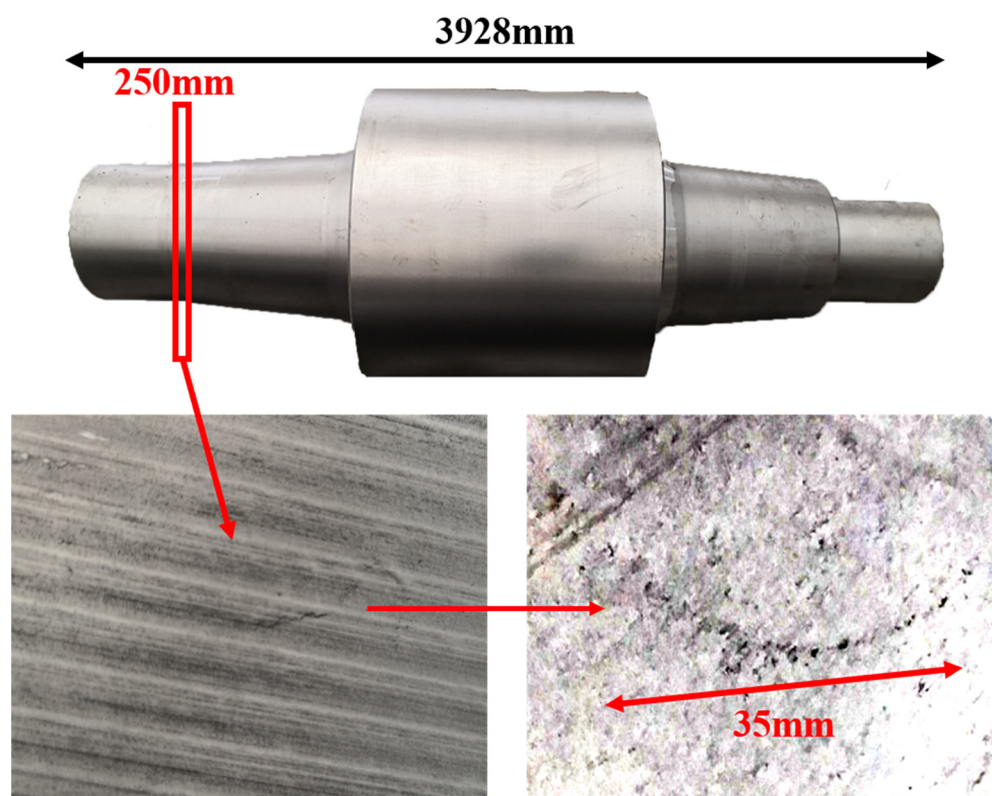

Figure 1. Schematic illustration of original metallurgical process and sampling.

Figure 2. Sampling and defective part characteristics on the roller.

2.2. Analysis Method of Composition and Micro-Inspection

The [Si], [Mn], [Al], [Ca] contents in molten steel were determined by inductively coupled plasma optical emission spectrometer method (ICP-OES). (ThermoFisher, Waltham, MA, USA) The total oxygen contents were analyzed by the inert gas fusion-infrared absorptiometry method with an accuracy of ±0.0001%. The compositions of slag specimens that corresponded with steel specimens, respectively, were determined by X-ray fluorescence spectrometer (XRF). (PANalytical B.V., Almelo, The Netherlands) Additionally, the steel specimens were all well-ground and polished for the following micro-inspection. Scanning electron microscopy (SEM) (FEI, Hillsboro, OR, USA) and energy-dispersive X-ray spectroscopy (EDS) (Bruker, Billerica, MA, USA) for the micro-inspection. The maximum diameter of inclusions was considered as the size of the inclusions. Afterward, the composition of steel and slag specimens is shown in Tables 1 and 2, respectively.

Table 1. Main chemical composition of steel specimens in mass %.

Specimen No.	Stage	C/%	Si/%	Mn/%	P/%	S/%	Cr/%	Al/%	Ca/%	O/%
A1	IF-end	0.407	0.23	0.29	0.0095	0.0034	3.32	0.0018	0.0003	0.0242
A2	LF1-initial	0.422	0.22	0.29	0.0092	0.0034	3.27	0.0015	0.0008	0.0285
A3	LF1-end	0.433	0.19	0.32	0.0098	0.0025	3.30	0.0036	0.0003	0.0045
A4	LF2-initial	0.423	0.17	0.32	0.0098	0.003	3.24	0.0032	0.0003	0.0067
A5	LF2-end	0.519	0.49	0.60	0.0113	0.0005	5.20	0.0076	0.0062	0.0021
A6	VD-end	0.539	0.46	0.60	0.0112	0.0004	5.20	0.0063	0.0012	0.0022
A7	LF3-end	0.538	0.47	0.60	0.0113	0.0004	5.25	0.0067	0.0017	0.0017
A8	VC- initial	0.536	0.47	0.60	0.0117	0.0006	5.27	0.0062	0.0006	0.002

Table 2. Main chemical composition of slag specimens in mass %.

Specimen No.	Stage	CaO	SiO$_2$	Al$_2$O$_3$	MnO	Cr$_2$O$_3$	FeO	CaF$_2$
A1	IF-end	5.91	46.30	19.90	13.30	6.08	3.51	0.17
A2	LF1-initial	6.62	42.20	19.10	11.70	7.19	3.63	0.32
A3	LF1-end	63.17	19.40	6.48	0.16	0.14	0.48	3.86
A4	LF2-initial	—	—	—	—	—	—	—
A5	LF2-end	61.69	19.30	4.55	0.03	0.04	0.25	8.07
A6	VD-end	58.91	20.80	6.51	0.02	0.03	0.16	7.06
A7	LF3-end	58.25	19.10	6.99	0.04	0.05	0.38	7.98
A8	VC- initial	57.83	19.10	6.50	2.30	0.05	0.35	7.59

3. Results

3.1. Analysis of Defective Part on the Ingot

The defective parts that failed the magnetic particle inspection test were investigated through SEM and EDS analysis method, which is shown in Figure 3. A linear and aggregating defect up to 3 mm was observed, which could lead to the failure of flaw detection directly, as shown in Figure 3a. Based on the element mapping of defects, the linear and aggregating defect is composed of single SiO$_2$-MnO-Al$_2$O$_3$ inclusion, which presented irregular in shape and uneven in size, as shown in Figure 3b. The morphology and element mapping of single and large-size inclusions are shown in Figure 3c,d, respectively. The large SiO$_2$-MnO-Al$_2$O$_3$ inclusion that demonstrated in irregular plate strip is up to nearly 372 μm. In general, the SiO$_2$-MnO-Al$_2$O$_3$ type inclusions considered as easily deformable have a low liquidus temperature and contact angle, which could increase difficulties of the removal by its floatation [31–33]. Besides, large-size inclusions, e.g., SiO$_2$-MnO-Al$_2$O$_3$, CaO-SiO$_2$-Al$_2$O$_3$ inclusions with low contact angles were also considered to have a poor tendency of agglomeration [34]. However, Vantilt et al. [32] found the cluster and agglomeration of liquid, spherical SiO$_2$-MnO-Al$_2$O$_3$ inclusions driven by the capillary depression forces. The morphological difference of SiO$_2$-MnO-Al$_2$O$_3$ inclusions from spherical to irregular was suggested as the result of forging. In summary, it could be suggested that the formation of the large-size and aggregating SiO$_2$-MnO-Al$_2$O$_3$ type inclusions led to the failure in the previous MPI test.

3.2. Characteristics of the Inclusions during the Metallurgical Process

To clarify the origin and formation of large-size SiO$_2$-MnO-Al$_2$O$_3$ type inclusions in molten steel, the evolution of inclusions during the metallurgical process was investigated through SEM and EDS analysis, especially for the large-size inclusions. Morphology and composition of typical large-size inclusions at different stages were shown in Table 3. Typical inclusions in specimen A1 (IF-end before tapping) were large-size spherical SiO$_2$-MnO-Al$_2$O$_3$ inclusions up to 30 μm, which were even-distributed in the composition based on the micrograph. After the tapping, the main inclusion type remained as SiO$_2$-MnO-Al$_2$O$_3$. In the meanwhile, a few CaO content appeared in some SiO$_2$-MnO-Al$_2$O$_3$ inclusions, and the shapes changed from sphere to non-smooth and irregular sphere. After the addition of Si-Al complex deoxidizer during the following LF1 and LF2 refining process, the main inclusions converted into CaO-SiO$_2$-Al$_2$O$_3$ type with a low liquidus temperature and contact angle as well [31,34]. Additionally, only a few SiO$_2$-MnO-Al$_2$O$_3$ inclusions with decreasing sizes were found at the end of the LF2 refining process. After the breaking of VD, the CaO- SiO$_2$- Al$_2$O$_3$ inclusions were observed as a minor part. The main inclusion changed from CaO-SiO$_2$-Al$_2$O$_3$ to SiO$_2$-MnO-Al$_2$O$_3$ type. In the following LF3 refining and VC casting process, the main inclusion remained still as CaO-SiO$_2$-Al$_2$O$_3$. In the meanwhile, SiO$_2$-MnO-Al$_2$O$_3$ type became minor with decreasing sizes gradually.
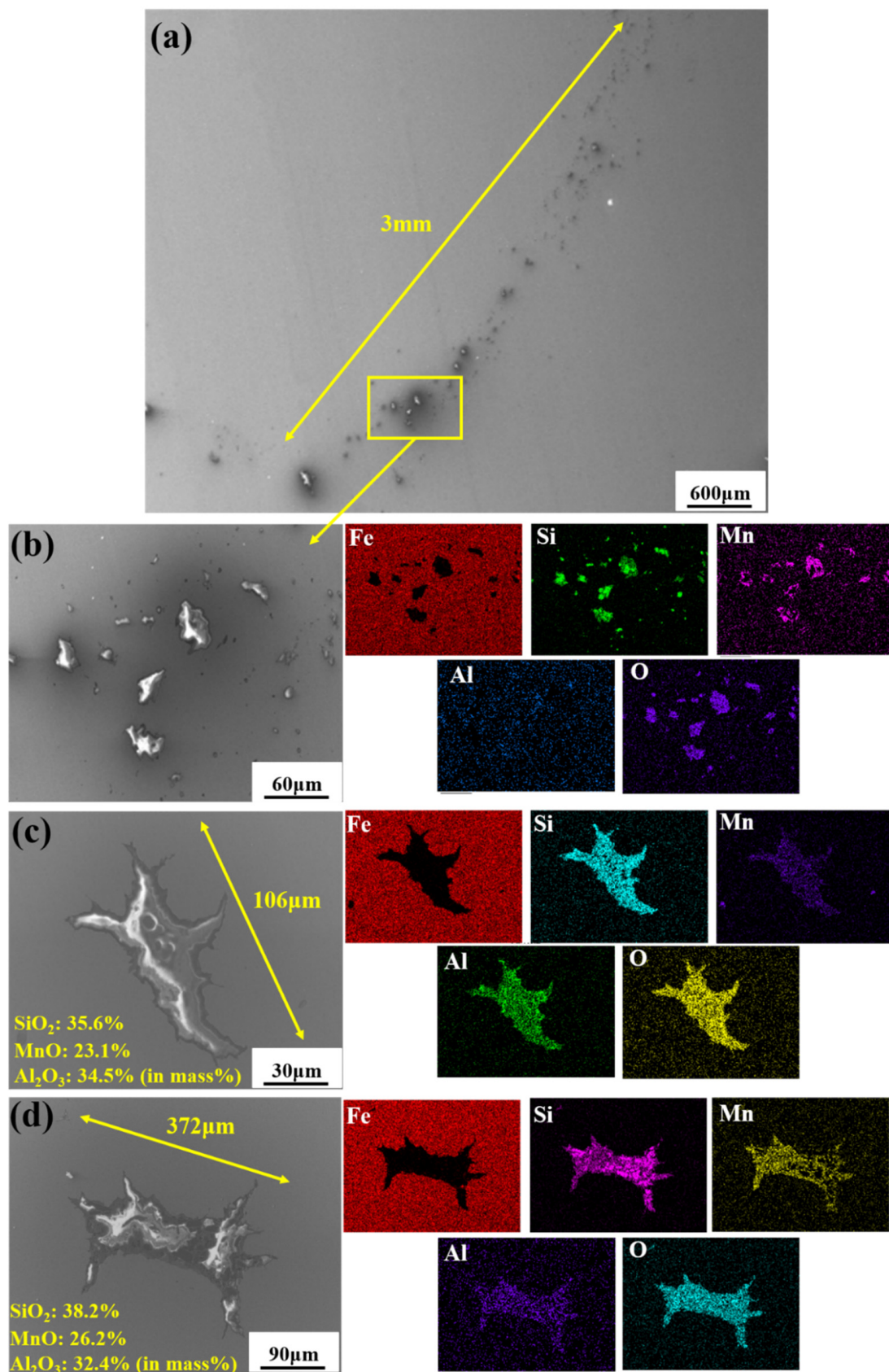
Figure 3. Morphology and element mapping of the defective area on the near surface of ingot. (**a**) morphology of defects in overall; (**b**) clusters of SiO_2-MnO-Al_2O_3 inclusions; (**c**,**d**) large-size single SiO_2-MnO-Al_2O_3 inclusion.

Table 3. Morphology and composition (in mass%) of typical large-size inclusions at different stages (Specimen A1–A8).

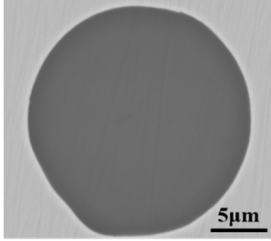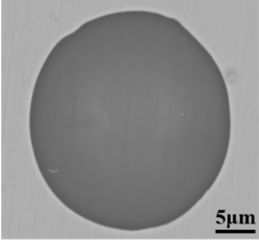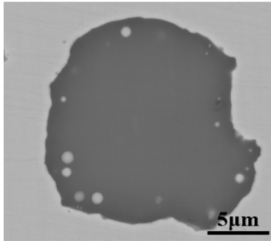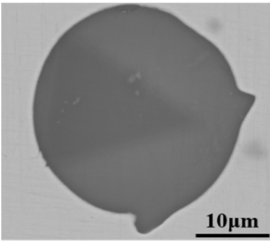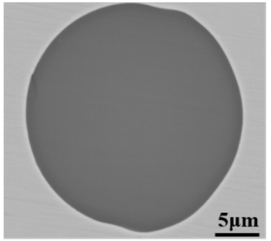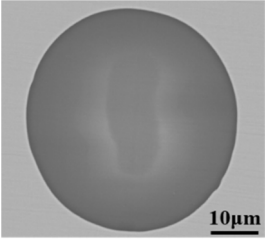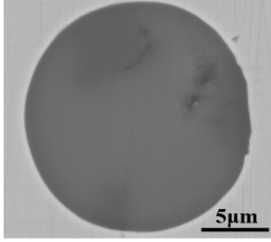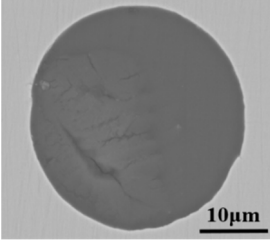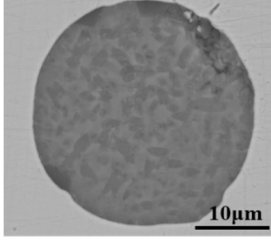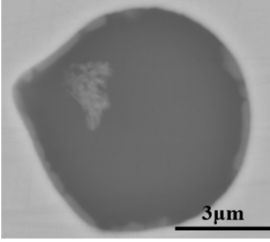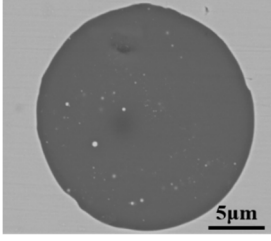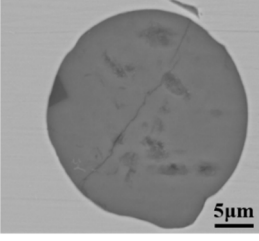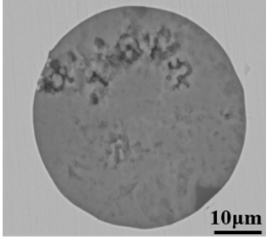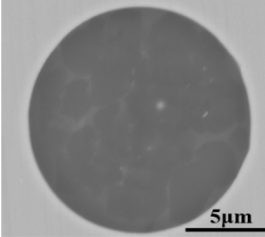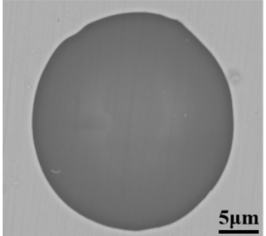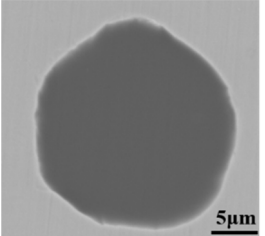| Sample No.	Stage	Main Inclusions		Minor Inclusions	
		Morphology	Type wt.%	Morphology	Type wt.%
A1	IF-end		SiO_2-(48.0%) MnO-(22.3%) Al_2O_3-(29.6%)		SiO_2-(72.4%) MnO-(18.6%) Al_2O_3-(0.09%)
A2	LF1-intial		SiO_2-(28.2%) MnO-(14.2%) Al_2O_3-(46.5%) CaO-(10.5%)		SiO_2-(58.1%) MnO-(12.3%) Al_2O_3-(29.6%)
A3	LF1-end		CaO-(11.2%) SiO_2-(49.3%) Al_2O_3-(39.5%)		CaO-(50.7%) SiO_2-(33.6%) Al_2O_3-(15.7%)
A4	LF2- initial		CaO-(24.4%) SiO_2-(24.4%) Al_2O_3-(51.2%)		CaO-(36.2%) SiO_2-(26.9%) Al_2O_3-(36.9%)
A5	LF2-end		CaO-(79.0%) SiO_2-(10.0%) Al_2O_3-(11%)		SiO_2-(42.0%) MnO-(22.5%) Al_2O_3-(35.0%)
A6	VD-end		SiO_2-(72.5%) MnO-(22.3%) Al_2O_3-(5.1%)		CaO-(75.7%) SiO_2-(18.5%) Al_2O_3-(5.9%)

Table 3. *Cont.*

Sample No.	Stage	Main Inclusions		Minor Inclusions	
		Morphology	Type wt.%	Morphology	Type wt.%
A7	LF3-end		CaO-(63.8%) SiO$_2$-(18.2%) Al$_2$O$_3$-(18.0%)		SiO$_2$-(25.0%) MnO-(22.3%) Al$_2$O$_3$-(54.2%)
A8	VC-initial		CaO-(52.6%) SiO$_2$-(12.6%) Al$_2$O$_3$-(34.8%)		SiO$_2$-(15.0%) MnO-(12.3%) Al$_2$O$_3$-(72.5%)

To illustrate the evolution of large-size inclusions at a different stage, the composition and size of inclusions found in specimen A1–A8 were marked in the ternary diagram of CaO-SiO$_2$-Al$_2$O$_3$ and SiO$_2$-MnO-Al$_2$O$_3$ system utilizing Factsage 8.1 thermodynamics software, (version 8.1, CRCT, Montreal, Canada) as shown in Figure 4a–d, respectively. The isothermal temperature of each diagram was set as 1873 K. The red line represented the liquid oxide phase region. During the smelting process, a few inclusions are located in the liquid oxide phase. Inclusions were mainly distributed around CaO and SiO$_2$ corners in the CaO-SiO$_2$-Al$_2$O$_3$ ternary diagram shown in Figure 4a. At the end of the IF melting process, the composition of inclusions was mainly located in the SiO$_2$ corner with a certain amount of Al$_2$O$_3$. During the LF1 refining process, the inclusions were going to own higher Al$_2$O$_3$ and CaO contents gradually. Then, most inclusions found in the LF2-initial stage were mainly liquid oxide. However, the CaO content in the inclusions compared with the initial stage has risen rapidly till the end of LF2-end. Despite the slight decrease of CaO content in a few inclusions, however, the main inclusions with larger sizes were still found around the corner of SiO$_2$. Afterward, the composition of inclusions stayed roughly stable in the following process. Due to the limits of the ternary diagram, the composition of inclusions was also projected into the SiO$_2$-MnO-Al$_2$O$_3$ system to clarify the evolution of SiO$_2$-MnO-Al$_2$O$_3$ type inclusions, which were shown in Figure 4b,d. SiO$_2$-MnO-Al$_2$O$_3$ type inclusions were mainly found at the initial stage before the LF1 refining process. Meanwhile, the composition of SiO$_2$-MnO-Al$_2$O$_3$ inclusions found after the breaking of VD were similar to the ones at the IF-end. Moreover, the composition of SiO$_2$-MnO-Al$_2$O$_3$ in the defective area marked in Figure 4b was located in the liquid oxide phase.

The size of inclusions was represented by the diameter of circles in the diagram as shown in Figure 4c,d, respectively, which were mainly spherical both in the CaO-SiO$_2$-Al$_2$O$_3$ and SiO$_2$-MnO-Al$_2$O$_3$ system. During the latter half of LF1 and the whole LF2 refining process, the sizes of inclusions were up to 30 μm owing to the collision, agglomeration, floatation, and absorption by high basicity slag. Super large-size inclusion up to 100 μm was only observed at the breaking of VD. The rest of the large-size inclusions were mainly located in dual-phase regions, which were around the corner of CaO and SiO$_2$. However, the sizes of inclusions found in the LF3-end and VC-initial were mostly rather smaller compared with VD-end ones. In addition, the sizes of pure liquid inclusions were relatively smaller. The SiO$_2$-MnO-Al$_2$O$_3$ inclusions were firstly observed at the stage of IF-end, then grew up bigger during the stage of the LF refining process. A huge amount

of large-sized SiO$_2$-MnO-Al$_2$O$_3$ inclusions that were unabsorbed and undissolved in the refining slag were found after the breaking of VD, which could lead to the failure of flaw detection directly.
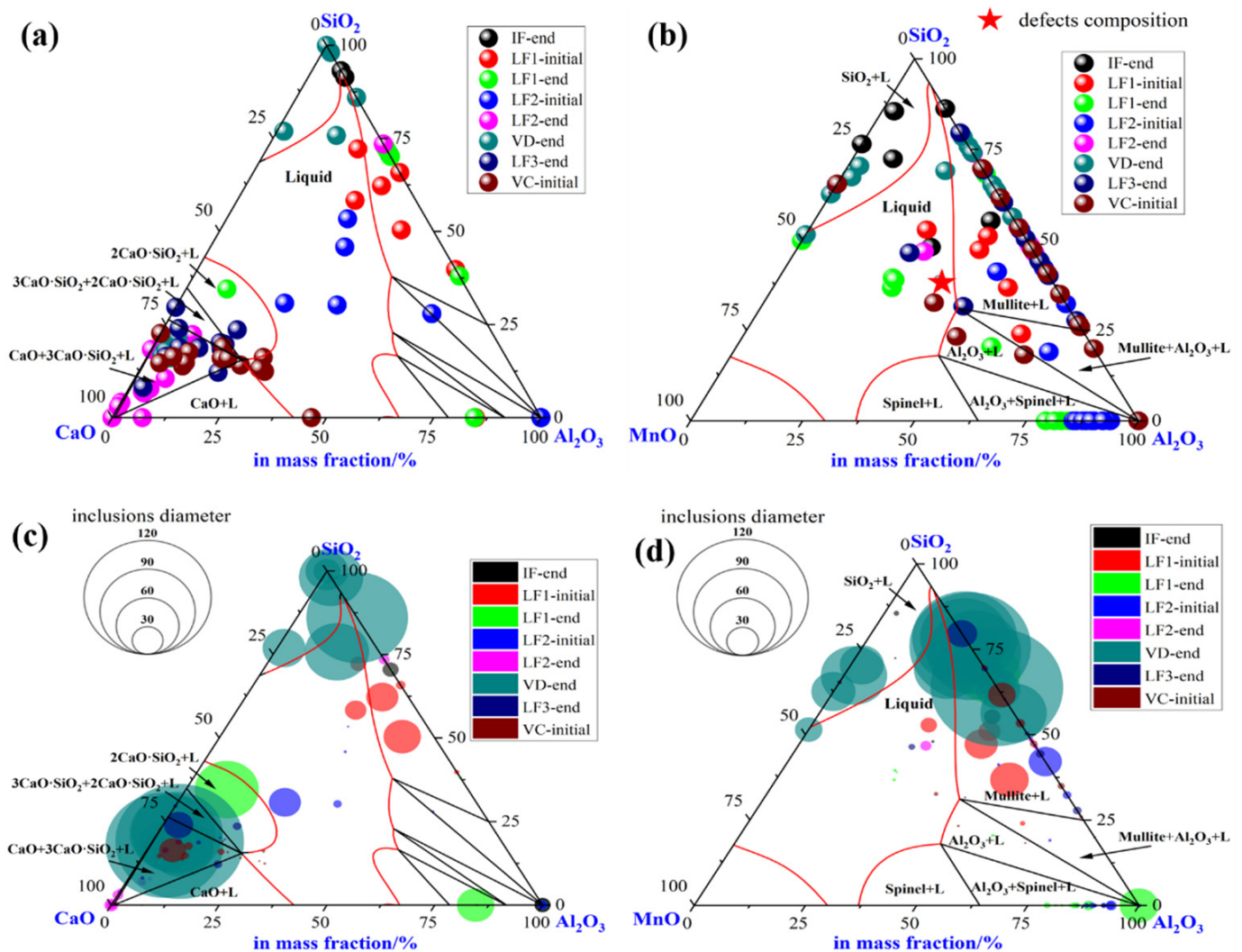
Figure 4. Composition and size distribution of inclusions during the metallurgical process in CaO-SiO$_2$-Al$_2$O$_3$ and SiO$_2$-MnO-Al$_2$O$_3$ ternary phase diagram at 1873 K. (**a**) Composition of inclusions in CaO-SiO$_2$-Al$_2$O$_3$ diagram, (**b**) composition of inclusions in SiO$_2$-MnO-Al$_2$O$_3$ diagram, (**c**) size distribution of inclusions in CaO-SiO$_2$-Al$_2$O$_3$ diagram, (**d**) size distribution of inclusions in SiO$_2$-MnO-Al$_2$O$_3$ diagram.

The type and the average size of all type inclusions at each stage was shown in Figure 5. The SiO$_2$-MnO-Al$_2$O$_3$ inclusions were found during the whole metallurgical process. The occurrence of Al$_2$O$_3$ and CaO-SiO$_2$-Al$_2$O$_3$ inclusions were presented as complementary. Owing to the incomplete deoxidation in the molten steel and stirring between slag and molten steel during the avoiding of the top slag process, the Al$_2$O$_3$ inclusions were found mostly before the LF2 refining process. Then the Al$_2$O$_3$ inclusions were modified into the MgO-Al$_2$O$_3$ spinel inclusions due to the dissolution of MgO-based refractory. The CaO-SiO$_2$-Al$_2$O$_3$ inclusions remained as the majority till the VC-initial stage. The average size of inclusions at the breaking of VD was much higher than the other stages owing to the appearance of the large amount, large-sized SiO$_2$-MnO-Al$_2$O$_3$ inclusions.
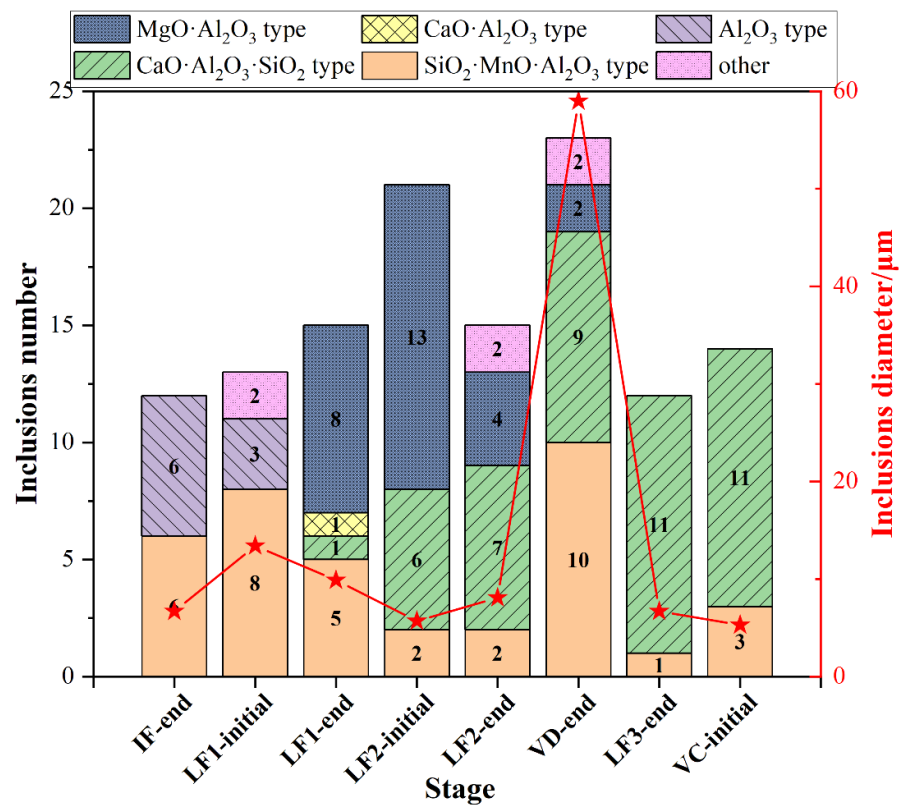
Figure 5. Type and average size distribution of all inclusions at different stages.

4. Discussion

4.1. Formation Mechanism of the SiO_2-MnO-Al_2O_3 Type Inclusions

Based on observation and analysis for the inclusions found in the metallurgical process, it could be inferred that the SiO_2-MnO-Al_2O_3 inclusions were formed at the end of IF, and remained in the following stages. To clarify the formation mechanism of the SiO_2-MnO-Al_2O_3 inclusion, the stability phase diagrams of the Si-Mn-O system in the Fe-5Cr back-up roller system were calculated through Factsage 8.1 software at different aluminum content (0, 0.003%, 0.007%, 0.01%, 0.015%). The colored dotted line represented different oxygen content in the molten steel, which was shown in Figure 6a–e, respectively. As shown in Figure 6a, at the 0 aluminum content, it could be found that liquid oxide, SiO_2, spinel (MnO-Cr_2O_3), and MnO phases in the molten steel with the content of silicon and manganese ranging from 1 ppm to 10% and 100 ppm to 10%, respectively. Besides, the regions of SiO_2, MnO, and liquid oxide phase became larger with the increasing oxygen content in the molten steel, which also indicated that the increasing degree of over-oxidation extended the formation scale of liquid oxide. The spinel and SiO_2 phase-field were modified into Al_2O_3 and mullite phase fields. The Al_2O_3+liquid oxide dual-phase field was formed in the previous pure liquid oxide phase-field region when the aluminum content increased to 30 ppm. Due to the similar aluminum content, the composition of A3 and A4, A5, and A6 were located in the dual-phase of Al_2O_3+liquid oxide and marked in Figure 6b,c, respectively. It could be indicated that the endogenous inclusions of each stage should be Al_2O_3+liquid oxide type, which was verified above. Due to the strong stirring of the VD process and the similar SiO_2-MnO-Al_2O_3 inclusions composition between IF-end and VD-end, as shown in Figure 5b, the SiO_2-MnO-Al_2O_3 inclusions found in the A6(VD-end) could be suggested as the result of slag entrapment containing unabsorbed or undissolved, large-sized SiO_2-MnO-Al_2O_3 inclusions. At a certain oxygen content in the molten steel, the region related to the liquid oxide became smaller with the increasing aluminum content. Consequently, it could be inferred that the aluminum content could promote the decrease of liquid oxide effectively.
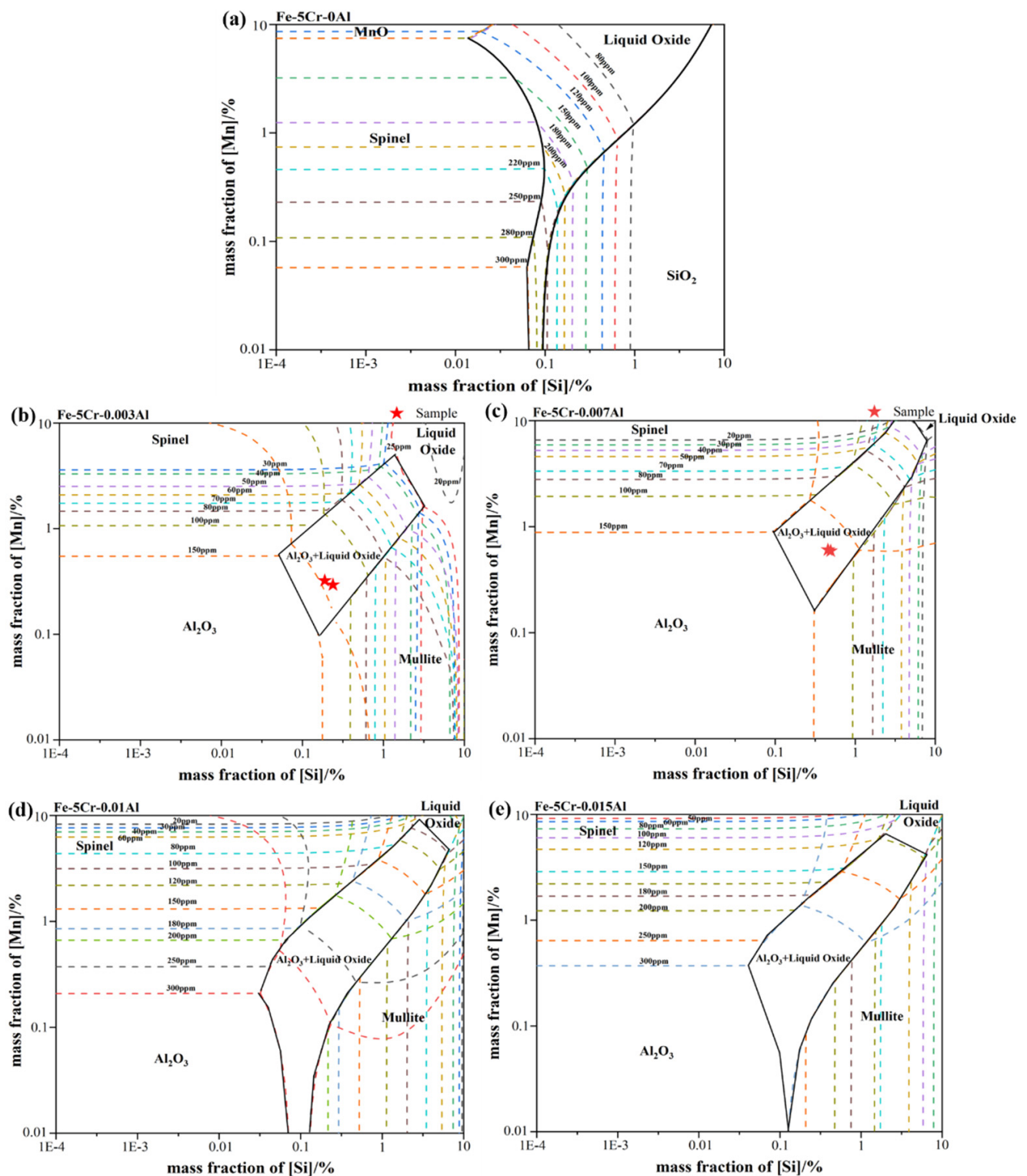
Figure 6. Calculated oxide stability diagrams of Si-Mn-O system with iso-oxygen contours (in ppm) in Fe-5Cr back-up roller at 1873 K: (**a**) with 0 Al (**b**) with 30 ppm Al (**c**) with 70 ppm Al (**d**) with 0.01% Al (**e**) with 0.015% Al.

4.2. Modification of the Liquid Oxide Inclusions

To obtain the quantitative relationship between the aluminum content and the formation of liquid oxide, the evolution of oxide inclusions in Fe-5Cr-0.55C-0.55Si-0.6Mn-6 ppm Ca containing different aluminum contents was calculated with the aid of Factsage

8.1 software, as shown in Figure 7. The FactIPS, FTmisc, and FToxide databases were used for calculation. The soluble oxygen contents in the molten steel ranged from 20 ppm to 200 ppm were shown in Figure 7a,c,e,g, respectively, which corresponded to the different stages in the smelting process. The upper and lower aluminum contents during the smelting process were marked in a blue dotted line. As shown in Figure 7g, at the oxygen content of 200 ppm in molten steel, the SiO_2, liquid oxide, and Al_2O_3 phase existed when the aluminum content was below 100 ppm corresponded to the actual value. The liquid oxide phase disappeared completely, which was replaced by the CA_6 (CaO-$6Al_2O_3$) phase till the aluminum content reached roughly 0.024%. Besides, the SiO_2, Al_2O_3, and MnO contents in the liquid oxide stayed as the dominating part, and the CaO content in liquid oxide stayed as a minor part. Then, the liquid oxide formed at 200 ppm oxygen content was determined as SiO_2-MnO-Al_2O_3 type inclusions which corresponded to the observed results above. Consequently, it could be inferred that a minimum of 0.024% aluminum content in the molten steel was required to convert the SiO_2-MnO-Al_2O_3 type liquid oxide into the high melting point Al_2O_3 inclusions, which were widely recognized as easier to remove by their floatation and slag absorption than liquid oxides did [34–37]. Generally, the contact angles of liquid oxide and solid oxide are below 90° and beyond 90° at 1873 K, respectively, which could reflect the difficulties of slag absorption. The liquid film was formed between the liquid inclusions and slag interface when the liquid inclusions were about to go through the slag-steel interface. Then the slow discharge of liquid film would take rather longer to get absorbed than the solid ones, in which no liquid film has been formed during the process. Then, it could be concluded that reducing of liquid oxide (SiO_2-MnO-Al_2O_3 and CaO-SiO_2-Al_2O_3 type) and modification to the Al_2O_3 type solid inclusions could promote the cleanness of molten steel effectively. The aluminum content required for the complete modification of solid Al_2O_3 type inclusions reduced from 0.024% to 0.01% when the oxygen level declined from 200 ppm to 50 ppm, which corresponded to the process of IF melting to LF refining, as shown in Figure 7c,d,e,f. However, in the meanwhile, the CaO content in liquid oxide has risen higher than MnO at the 50 ppm oxygen content in molten steel, which meant the newly formed liquid oxide transformed from SiO_2-MnO-Al_2O_3 type to CaO-SiO_2-Al_2O_3 type corresponding to the analysis in the LF2-refining process. In addition, the newly formed stable phases were converted to CA_2 (CaO-$2Al_2O_3$) and $CA6$ (CaO-$6Al_2O_3$) phases by the effect of high basicity slag. The required aluminum content for the complete modification rose to 0.02% at the 20 ppm oxygen content in molten steel, which represented the end of the LF refining process in the plant trial. Due to the modification of the high basicity slag and complete oxidation in molten steel, the solid inclusions were converted into pure CA_2 inclusion. The content of CaO in liquid oxide has risen higher than SiO_2 gradually, as shown in Figure 7a,b. Above all, it could be suggested that a minimum of 0.024% aluminum content could minimize the formation of SiO_2-MnO-Al_2O_3 liquid oxide before the tapping. Besides, maintaining the aluminum content beyond 0.02% in the whole refining process could also minimize the formation of CaO-SiO_2-Al_2O_3 liquid oxide.

4.3. Optimization and Verification of Plant Trials

Based on the results and analysis above, the authors brought the aluminum control over the whole smelting process into effect to solve the flaw detection issues caused by SiO_2-MnO-Al_2O_3 type inclusions, as shown in Figure 8. Meanwhile, the composition of slag was redesigned to match both the high aluminum content in molten steel and the refining function. Then, the steel specimens corresponding to the previous stages were also sampled and analyzed as above. Specific details of sampling in the optimized plant trial are shown in Figure 8. The composition of slag specimens in the optimized process is shown in Table 4.
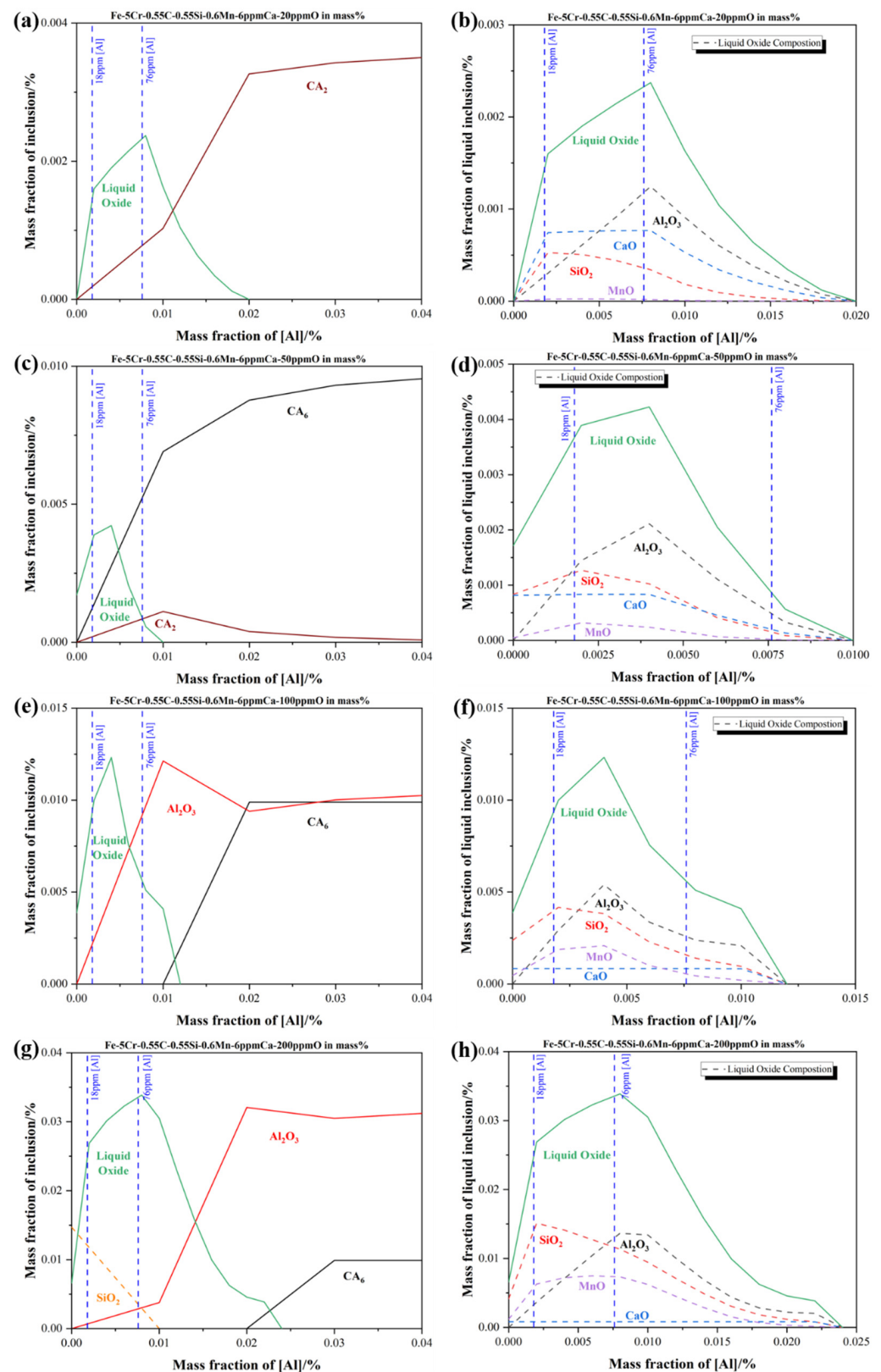
Figure 7. Equilibrium formation of inclusions during different soluble oxygen content stages at 1873 K in Fe-5Cr-0.55C-0.55Si-0.6Mn-6 ppm Ca-Al in mass % (**a**,**b**) with 20 ppm (**c**,**d**) with 50 ppm (**e**,**f**) with 100 ppm (**g**,**h**) with 200 ppm (**a**,**c**,**e**,**g**) present the formation of all inclusions at different oxygen content (**b**,**d**,**f**,**h**) present the actual composition of liquid oxide inclusions corresponding to the previous one, respectively.
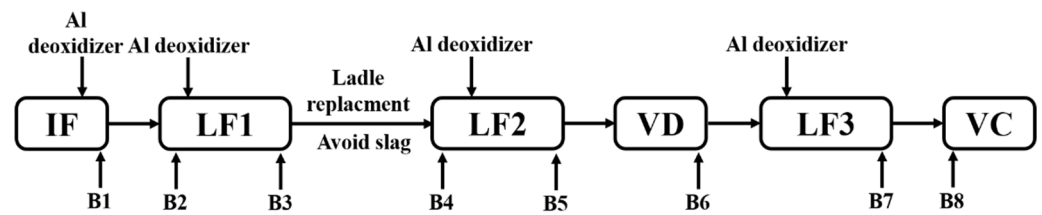
Figure 8. Schematic illustration of optimized metallurgical process and sampling.

Table 4. Main chemical composition of slag specimens in the optimization process in mass%.

Specimen No.	Stage	CaO	SiO$_2$	Al$_2$O$_3$	MnO	Cr$_2$O$_3$	FeO	CaF$_2$
B1	IF-end	0.99	41.00	19.00	20.40	10.00	3.82	0.00
B2	LF1-initial	2.36	31.80	36.50	13.60	6.51	3.90	0.08
B3	LF1-end	62.79	16.70	10.60	0.20	0.15	0.57	4.19
B4	LF2-initial	—	—	—	—	—	—	—
B5	LF2-end	54.39	12.00	23.20	0.15	0.20	1.07	2.24
B6	VD-end	53.07	11.30	24.50	0.05	0.10	0.47	2.13
B7	LF3-end	53.33	11.10	24.80	0.05	0.10	0.46	1.97
B8	VC- initial	52.88	11.00	25.20	0.07	0.12	0.80	2.01

Morphology and composition of improved typical inclusions at different stages were shown in Table 5. Only aggregating and irregular Al$_2$O$_3$ particles were found before the LF1 refining process. Then, pure Al$_2$O$_3$ particles were modified into small-sized and quasi-spherical CaO-Al$_2$O$_3$ type inclusions in the LF refining process. However, the CaO-Al$_2$O$_3$ type inclusions were modified into CaO-SiO$_2$-Al$_2$O$_3$ type inclusions after the breaking of the VD process. The CaO-SiO$_2$-Al$_2$O$_3$ type inclusions remained as the main inclusions till the casting of the VC process. To illustrate the optimized evolution of large-size inclusions at different stages, the composition and size of inclusions found in specimens B1-B8 were marked in the ternary diagram of the CaO-SiO$_2$-Al$_2$O$_3$ system, as shown in Figure 9. During the whole smelting process, a few inclusions were located at the line of SiO$_2$-Al$_2$O$_3$, which meant few SiO$_2$-MnO-Al$_2$O$_3$ type inclusions were found. Large-sized inclusions were mostly located in the liquid oxide and liquid oxide+CaO dual-phase field, which was relatively smaller than the SiO$_2$-MnO-Al$_2$O$_3$ type ones. Besides, large-sized inclusions were CaO-Al$_2$O$_3$ type at the end of LF2 refining. However, the liquid oxides were mostly converted to CaO-SiO$_2$-Al$_2$O$_3$, which were formed after the breaking of VD. It could be suggested that the inclusions with the tendency of high Al$_2$O$_3$ content usually owned small sizes. On the contrary, the inclusions with the tendency of high CaO content or a certain SiO$_2$ content owned larger sizes generally in this study. Fewer inclusions were found than the original process especially the SiO$_2$-MnO-Al$_2$O$_3$ type, which caused the failure of the MPI test. It showed that the modification of aluminum in the over-oxidation environment before the tapping was effective in a certain degree. In addition, the amount and sizes of inclusions in the optimized process were smaller than the previous ones.

Table 5. Morphology and composition (in mass %) of typical inclusions at different stages (Specimen B1–B8).
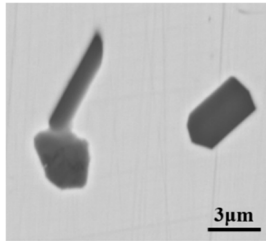
Specimen No.	Stage	Main Inclusions	
		Morphology	Type wt.%
B1	IF-end		Al$_2$O$_3$

Table 5. *Cont.*
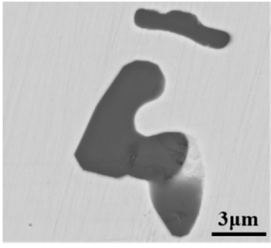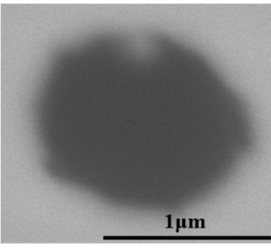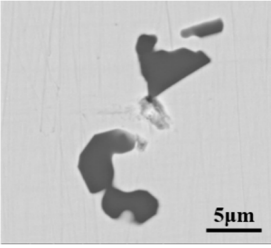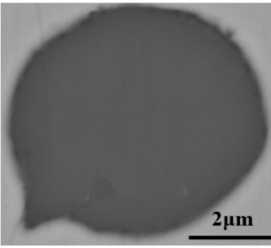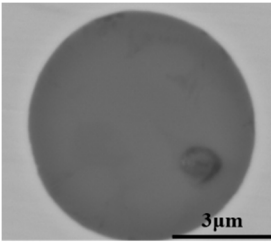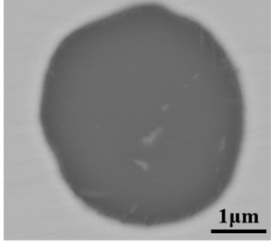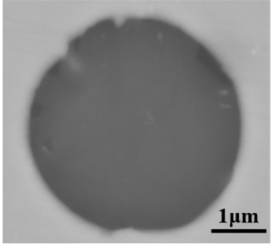
Specimen No.	Stage	Main Inclusions	
		Morphology	Type wt.%
B2	LF1-initial		Al_2O_3
B3	LF1-end		CaO-(11.2%) Al_2O_3-(83.2%)
B4	LF2-initial		Al_2O_3
B5	LF2-end		CaO-(57.6%) Al_2O_3-(40.2%)
B6	VD-end		CaO-(66.5%) SiO_2-(8.6%) Al_2O_3-(25.9%)
B7	LF3-end		CaO-(55.8%) SiO_2-(9.2%) Al_2O_3-(36.0%)

Table 5. *Cont.*

Specimen No.	Stage	Main Inclusions	
		Morphology	Type wt.%
B8	VC-initial		CaO-(40.9%) SiO$_2$-(6.4%) Al$_2$O$_3$-(52.7%)
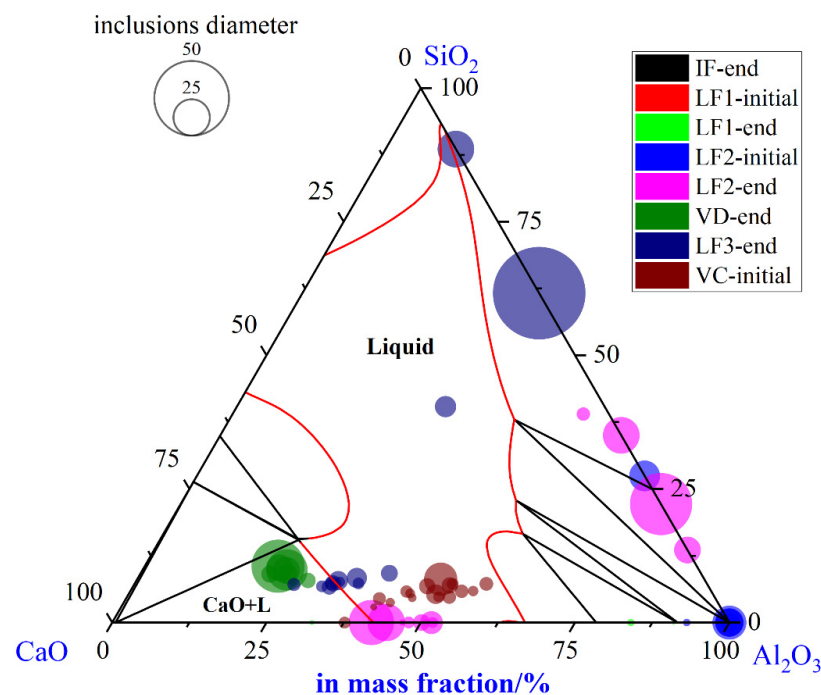
Figure 9. Composition and size distribution of large-size inclusions during the optimized metallurgical process in CaO-SiO$_2$-Al$_2$O$_3$ ternary phase diagram at 1873 K.

The type and the average size of all type inclusions at each stage was shown in Figure 10. SiO$_2$-MnO-Al$_2$O$_3$ inclusions were found after the LF2-initial stage, which could be entrapped from the slag during the avoiding slag process. Owing to the optimized control of aluminum content, Al$_2$O$_3$ inclusions dominated in inclusions before LF-2 refining, which were modified by the calcium content in the high basicity slag. Besides, the inclusion found at the breaking of VD owned larger sizes than other stages. The appearance of Al$_2$O$_3$ and CaO-SiO$_2$-Al$_2$O$_3$ inclusions was also presented as complementary, which matched the previous results. However, more CaO-SiO$_2$-Al$_2$O$_3$ inclusions were found after the breaking of the VD process than the previous ones. Therefore, the relationship between SiO$_2$, Al$_2$O$_3$ content in the inclusions, and the aluminum content in the molten steel was illustrated and shown in Figure 11. The SiO$_2$ contents in the inclusions and the aluminum content in the molten steel presented a negative correlation. At the end of LF2 refining, the SiO$_2$ contents in the inclusions were almost none. However, the Al$_2$O$_3$ contents of the inclusions decreased rapidly when the smaller SiO$_2$ contents increased. The SiO$_2$ contents decreased gradually after adding in the aluminum wire (aluminum 99%). Consequently, it could be inferred that the aluminum contents in the molten steel could suppress the formation of SiO$_2$ contents in the CaO-SiO$_2$-Al$_2$O$_3$ inclusions to a certain degree. However, the precise inner mechanism requires further investigation [38].
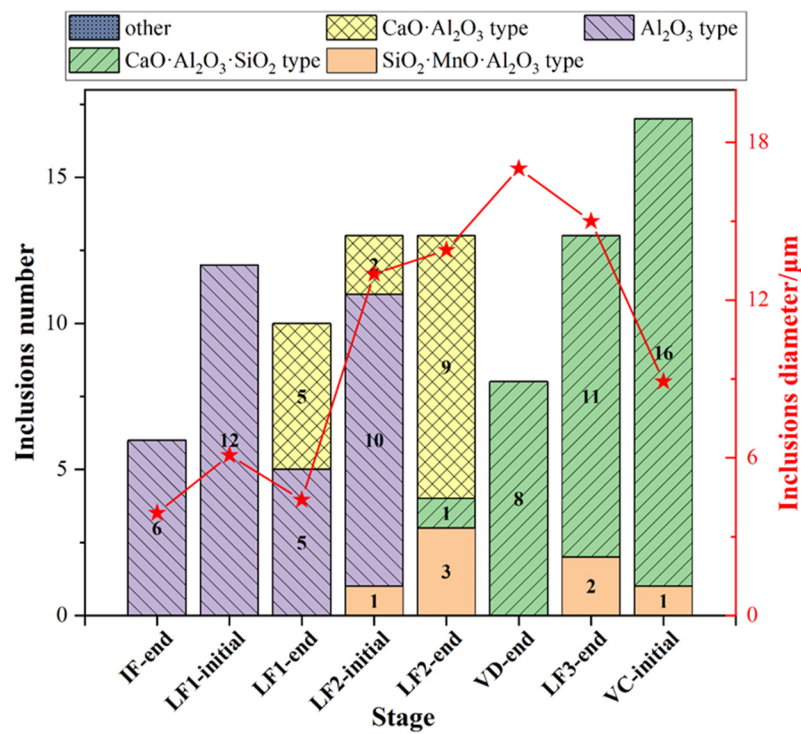
Figure 10. Type and average size distribution of all inclusions at different stages in the optimized plant trial.
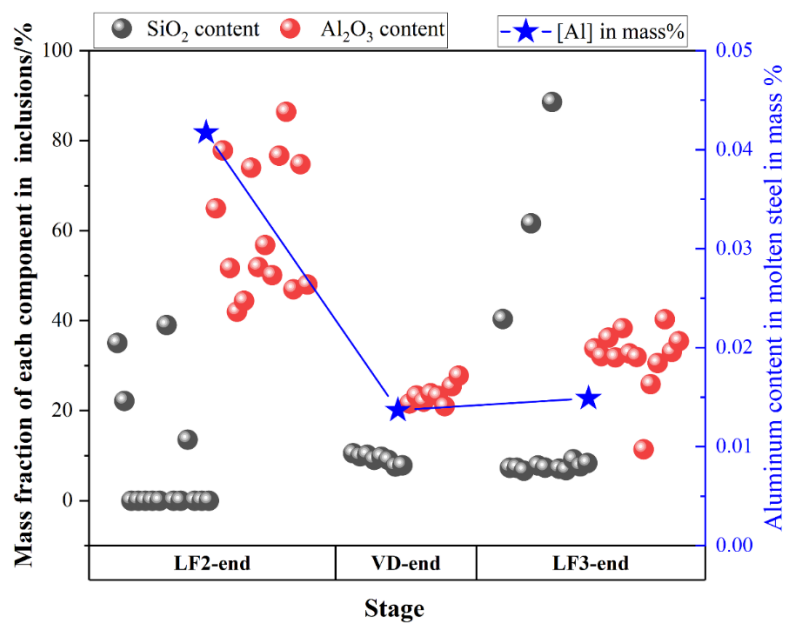

Figure 11. Mass fraction of SiO_2 and Al_2O_3 contents in the inclusions and the corresponding aluminum content during LF2-end, VD-end, LF3-end stage.

According to the experimental results and thermodynamic calculation, the formation and evolution mechanism of typical inclusions during the original and optimized metallurgical process were illustrated and shown in Figure 12. The scarps and alloys were melted by IF under the atmosphere. Then there would be a huge amount of FeO, MnO, and Cr_2O_3 oxide formed and entered into the top slag, which provided the oxygen content into the molten steel. If there were insufficient aluminum content in the molten steel, the huge number of SiO_2-MnO-Al_2O_3 inclusions would be formed by the joint control of silicon, manganese, and aluminum over the oxygen content in the molten steel, which

was not easy to remove by its floatation and the absorption of the slag. In the refining stage, the CaO content would emerge in both the SiO_2-MnO-Al_2O_3 and Al_2O_3 inclusions by the modification of the high basicity slag. Besides, the CaO-Al_2O_3 type inclusions were converted into CaO-SiO_2-Al_2O_3 inclusions owing to the insufficient aluminum content caused the aluminum loss during the VD process and the slag entrapment [39–41]. The precise and inner mechanism of these requires further investigation in the next stage.
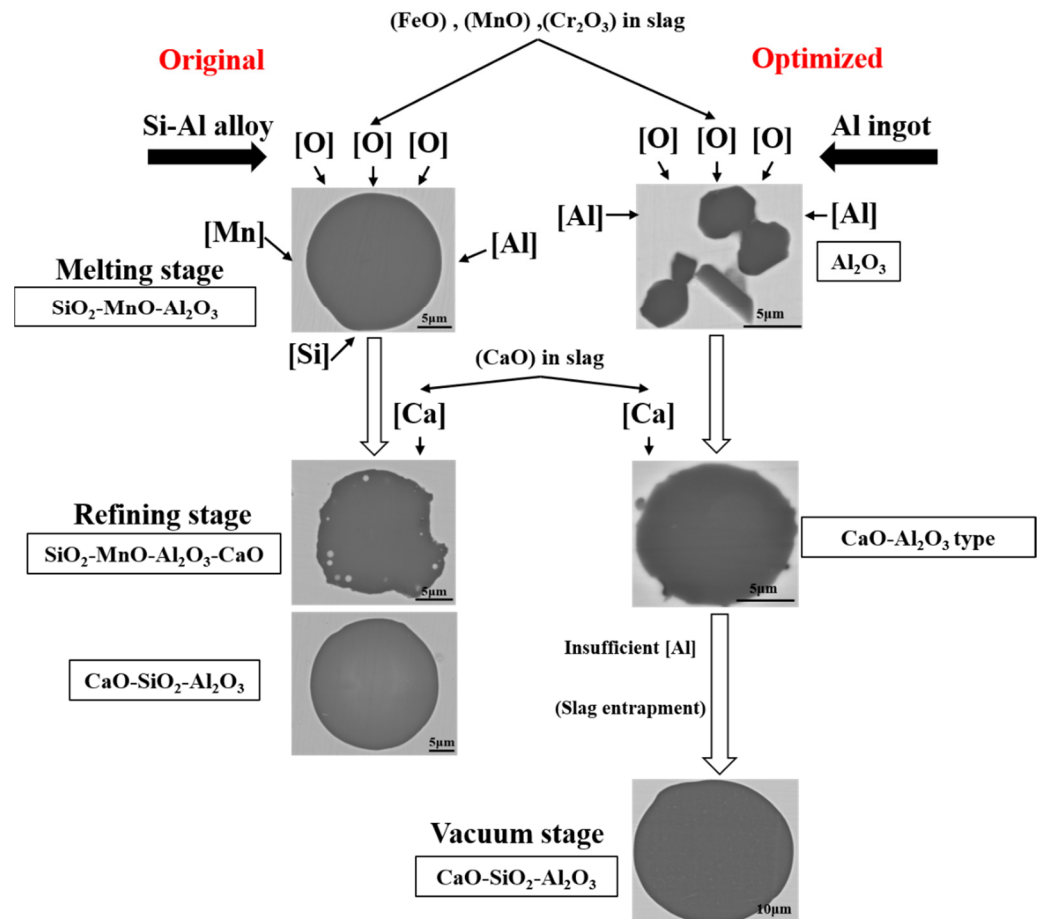
Figure 12. Schematic of formation and evolution of typical inclusions during the original and optimized metallurgical process.

5. Conclusions

In the current study, the source and formation of the defects that failed in the MPI test in forged backup rollers were investigated and the corresponding optimized process in the plant trials was conducted. Based on the analysis of inclusions characteristics and thermodynamic calculations, the conclusions were obtained as follows:

(1) The linear and aggregating distribution of SiO_2-MnO-Al_2O_3 inclusions up to 3 mm was the cause of the failure in flaw detection. The sizes of SiO_2-MnO-Al_2O_3 were rather uneven. Besides, SiO_2-MnO-Al_2O_3 inclusions with irregular plate strip shapes were uniformly distributed in composition.

(2) SiO_2-MnO-Al_2O_3 type inclusions were mainly formed in the over-oxidation environment during the IF melting. Owing to its low contact angles, large-size SiO_2-MnO-Al_2O_3 inclusions in the defective area were inherited from the initial smelting process. CaO-SiO_2-Al_2O_3 inclusions formed during the LF refining process were the dominating inclusions in the whole process.

(3) The content of aluminum in the molten steel over 0.024% in Fe-5Cr back-up roller steel could suppress the formation of SiO_2-MnO-Al_2O_3 liquid oxide during an over-oxidation environment. CaO-SiO_2-Al_2O_3 liquid oxide inclusions could be completely

modified as solid $CaO-Al_2O_3$ type inclusions over 0.02% aluminum content during the refining process. After the optimization, the amount and sizes of large-size liquid inclusions (>50 μm) decreased significantly before the VD refining.

References

1. Yu, S.D.; Chen, H. Current Status and Several Problems of Roller Industry in China. *Iron Steel* **2007**, *42*, 1–6.
2. Montmitonnet, P.; Buessler, P. A Review on Theoretical Analyses of Rolling in Europe. *ISIJ Int.* **1991**, *31*, 525–538. [CrossRef]
3. Gonzalez, W.B.; Llano, J.; García, J. *Metallurgical Application to Work and Back Up Rolls for Hot & Cold Rolling of Flat Products*; Rolls for Flat Rolling of Steel: Lugones, Spain, 2007.
4. Mammeri, A.; Belzune, F.J.; Rodirguez, C.; Torre, M.; Poveda, S.; Garcia, J. Mechanical Properties of Chromium Steels for Back up Rolling Rolls. *Rev. Metal.* **2003**, *39*, 107–113. [CrossRef]
5. Nakagawa, Y.; Hashimoto, T.; Katayama, H.; Morikawa, H. Development of High-Cr Roll for Hot Strip Mill with Superior Resistance to Surface Deterioration and Spalling of Outer Shell. *Tetsu-to-Hagane* **1988**, *74*, 1993–2000. [CrossRef]
6. Shimizu, M.; Shitamura, O.; Matsuo, S.; Kamata, T.; Kondo, Y. Development of High Performance New Composite Roll. *ISIJ Int.* **1992**, *32*, 1244–1249. [CrossRef]
7. Di Schino, A.; Di Nunzio, P.E. Metallurgical Aspects Related to Contact Fatigue Phenomena in Steels for Back-Up Rolls. *Acta Metall. Slovaca* **2017**, *23*, 62–71. [CrossRef]
8. Jia, R.; Li, X.D.; Li, J.C.; Gu, K. Present Research Situation on Cr5 Series Large Back-up Roll Process in China. *Hot Work. Technol.* **2013**, *42*, 62–65.
9. Mccann, J. Overview of Work Rolls for Cold Rolling. *Ironmak. Steelmak.* **2000**, *27*, 15–18.
10. Kang, X.; Li, D.; Xia, L.; Campbell, J.; Li, Y. Development of Cast Steel Back-up Roll. *Int. J. Cast Met. Res.* **2006**, *19*, 66–71. [CrossRef]
11. Ichino, K.; Ishikawa, S.; Kataoka, Y.; Toyooka, T. Improvement of Hot Wear Characteristic of High Speed Tool Steel Roll by Increase in Cr and Mo Contents. *Tetsu-to-Hagane* **2003**, *89*, 680–685. [CrossRef]
12. Yu, H.; Ji, C.; Chen, B.; Wang, C.; Zhang, Y. Characteristics and Evolution of Inclusion Induced Surface Defects of Cold Rolled IF Sheet. *J. Iron Steel Res. Int.* **2015**, *22*, 17–23. [CrossRef]
13. Sano, Y.; Hattori, T.; Haga, M. Characteristics of High-Carbon High Speed Steel Rolls for Hot Strip Mill. *ISIJ Int.* **1992**, *32*, 1194–1201. [CrossRef]
14. Kobayashi, K. Technical View on Forged Steel Rolls in Japan. *Tetsu-to-Hagane* **1971**, *57*, 725–737. [CrossRef]
15. Chen, J.L. Development of Cr5 Forged Blank of Cold-Rollers. *Forg. Stamp. Technol.* **2006**, *31*, 10–12.
16. Zhou, Q.; Zhang, J.; Yin, Y.; Zhai, M. Characterization of Inclusions in Axle Steel by Ingot Casting. *Metall. Res. Technol.* **2019**, *116*, 501–508. [CrossRef]
17. Huang, H.G.; Du, F.S.; Zhang, F. FEM Analyses on Forming Mechanics of Inclusion Defects Inner Heavy Backup-Roll Forging. *China Mech. Eng.* **2009**, *20*, 477–481.
18. Dong, B.L. Cause Analysis on Exposed Inclusion and Steel Melting Process Optimization of Backup Roll. *Heavy Cast. Forg.* **2019**, *40*, 46–48.
19. Gotoh, K.; Okada, H.; Sasaki, T.; Koide, T. Effects of Roll Surface Deteriorations on Scale Defect in Hot Rolling. *Tetsu-to-Hagane* **1998**, *84*, 861–867. [CrossRef]
20. Takechi, H.; Namba, K.; Kawasaki, K.; Fujiwara, K. Evaluation of the Fatigue Damage of Rolls for Strip Mills below the Surface by X-ray Diffraction Method. *Tetsu-to-Hagane* **1979**, *65*, 2067–2075. [CrossRef]

21. Ray, A.K.; Mishra, K.K.; Chaudhary, P.N. Failure Analysis of Rolls of Cold Rolling Mill in Steel Plant. In *Failure Analysis, Proceedings of the Clinic on Failure Analysis, Jamshedpur, India, 18–19 February 1997*; NML: Jamshedpur, India, 1997; pp. 37–46.
22. Wang, R.; Bao, Y.; Li, Y.; Yan, Z.; Li, D.; Kang, Y. Influence of Metallurgical Processing Parameters on Defects in Cold-Rolled Steel Sheet Caused by Inclusions. *Int. J. Miner. Metall. Mater.* **2019**, *26*, 440–446. [CrossRef]
23. Wang, Q.; Li, Z.; Shi, Y.; Wang, L.; Liu, F. Interior Crack and Its Formation Mechanism in Overlaying Weld of Back-up Rolls. *Eng. Fail. Anal.* **2013**, *34*, 268–277. [CrossRef]
24. Jamil, M.; Khan, A.M.; Hegab, H.; Sarfraz, S.; Sharma, N.; Mia, M.; Gupta, M.K.; Zhao, G.; Moustabchir, H.; Pruncu, C.I. Internal Cracks and Non-Metallic Inclusions as Root Causes of Casting Failure in Sugar Mill Roller Shafts. *Materials* **2019**, *12*, 2474. [CrossRef] [PubMed]
25. Lu, J.; Cheng, G.; Wu, M.; Yang, G.; Che, J. Detection and Analysis of Magnetic Particle Testing Defects on Heavy Truck Crankshaft Manufactured by Microalloyed Medium-Carbon Forging Steel. *J. Iron Steel Res. Int.* **2020**, *27*, 608–616. [CrossRef]
26. Wang, Q.; Cheng, G.; Li, J.; Dou, W.; Hu, X. Formation Mechanism of Large Inclusions in 80t 20Cr–8Ni Stainless Steel Casting for Nuclear Power. *Steel Res. Int.* **2019**, *90*, 1900349. [CrossRef]
27. Goto, K.; Matsuda, Y.; Sakamoto, K.; Sugimoto, Y. Basic Characteristics and Microstructure of High-Carbon High Speed Steel Rolls for Hot Rolling Mill. *ISIJ Int.* **1992**, *32*, 1184–1189. [CrossRef]
28. Lee, W.-H.; Liu, Y. Laboratory Evaluation of New Type of Backup Roll for Strip Shape Control. *ISIJ Int.* **2005**, *45*, 1636–1640. [CrossRef]
29. Prasad, M.S.; Ray, A.; Dhua, S.K.; Avtar, R.; Jha, S. Premature Failure of Work-Rolls in Tandem Mill: Some Microstructural Revelations. *J. Fail. Anal. Prev.* **2004**, *4*, 67–72. [CrossRef]
30. Kimura, T.; Ishii, M.; Amano, K.; Ueda, S.; Oka, Y.; Nakano, S. Secondary Hardening Characteristics and Those Effects on the Wear and Thermal Shock Resistance of 5%Cr-Mo-V Steel Roll for Cold Strip Mill. *ISIJ Int.* **1992**, *32*, 1224–1231. [CrossRef]
31. Parry, G.; Ostrovski, O. Wetting of Solid Iron, Nickel and Platinum by Liquid MnO–SiO2 and CaO–Al2O3–SiO2. *ISIJ Int.* **2009**, *49*, 788–795. [CrossRef]
32. Vantilt, S.; Coletti, B.; Blanpain, B.; Fransaer, J.; Wollants, P.; Sridhar, S. Observation of Inclusions in Manganese-Silicon Killed Steels at Steel-Gas and Steel-Slag Interfaces. *ISIJ Int.* **2004**, *44*, 1–10. [CrossRef]
33. Wang, K.; Jiang, M.; Wang, X.; Wang, Y.; Zhao, H.; Cao, Z. Formation Mechanism of SiO_2-Type Inclusions in Si-Mn-Killed Steel Wires Containing Limited Aluminum Content. *Metall. Mater. Trans. B* **2015**, *46*, 2198–2207. [CrossRef]
34. Shinozaki, N.; Echida, N.; Mukai, K.; Takahashi, Y.; Tanaka, Y. Wettability of Al_2O_3-MgO, ZrO_2-CaO, Al_2O_3-CaO Substrates with Molten Iron. *Tetsu-to-Hagane* **1994**, *80*, 748–753. [CrossRef]
35. Van Ende, M.-A.; Guo, M.; Proost, J.; Blanpain, B.; Wollants, P. Formation and Morphology of Al2O3 Inclusions at the Onset of Liquid Fe Deoxidation by Al Addition. *ISIJ Int.* **2011**, *51*, 27–34. [CrossRef]
36. Kapilashrami, E.; Sahajwalla, V.; Seetharaman, S. Investigation of the Wetting Characteristics of Liquid Iron on Mullite by Sessile Drop Technique. *ISIJ Int.* **2004**, *44*, 653–659. [CrossRef]
37. O'Malley, R.J. *Inclusion Evolution and Removal in Ladle Refining*; Missouri University of Science & Technology: Rolla, MO, USA, 2017.
38. Wu, S.; Guo, X.; Wang, Y.; Wu, G.; Lyu, S. Laboratory Study on Evolution Mechanism of Nonmetallic Inclusions in Al-Deoxidized Spring Steel. *Trans. Indian Inst. Met.* **2020**, *73*, 2807–2816. [CrossRef]
39. Kawakami, K.; Taniguchi, T.; Nakashima, K. Generation Mechanisms of Non-Metallic Inclusions in High-Cleanliness Steel. *Tetsu-to-Hagane* **2007**, *93*, 743–752. [CrossRef]
40. Deng, Z.; Zhu, M. Deoxidation Mechanism of Al-Killed Steel during Industrial Refining Process. *ISIJ Int.* **2014**, *54*, 1498–1506. [CrossRef]
41. Miao, Z.; Cheng, G.; Li, S.; Qiu, W.; Zeng, L.; Long, H. Formation Mechanism of Large-Size CaO–Al_2O_3–MgO–SiO_2 Inclusions in High Carbon Chromium Bearing Steel. *ISIJ Int.* **2021**, *61*, 2083–2091. [CrossRef]